PCCP

ARTICLE

Analysis of the interfacial characteristics of $BiVO_4$/metal oxide heterostructures and its implication on their junction properties

Received 00th January 20xx,
Accepted 00th January 20xx

DOI: 10.1039/x0xx00000x

www.rsc.org/

Yannick Hermans[ab], Sebastián Murcia-López[c], Andreas Klein[a], Roel van de Krol[d], Teresa Andreu[c], Joan Ramón Morante[c], Thierry Toupance[b], Wolfram Jaegermann[a,*]

The formation of heterostructures has proven to be a viable way to achieve high photoelectrochemical water splitting efficiencies with $BiVO_4$ based photoanodes. Especially, cobalt and nickel based oxides are suitable low cost contact materials. However, the exact role of these contact materials is not yet completely understood because of the difficulty to individually quantify the effects of surface passivation, charge carrier separation and catalysis on the efficiency of a heterostructure. In this study, we used photoelectron spectroscopy in combination with in-situ thin film deposition to obtain direct information on the interface structure between polycrystalline $BiVO_4$ and NiO, CoO_x and Sn-doped In_2O_3 (ITO). Strong upwards band bending was observed for the $BiVO_4$/NiO and $BiVO_4$/CoO_x interfaces without observing chemical changes in $BiVO_4$, while limited band bending and reduction of Bi and V was observed while forming the $BiVO_4$/ITO interface. Thus, the tunability of the Fermi level position within $BiVO_4$ seems to be limited to a certain range. The feasibility of high upwards band bending through junctions with high work function (WF) compounds demonstrate that nickel oxide and cobalt oxide are able to enhance the charge carrier separation in $BiVO_4$. Similar studies could help to identify whether new photoelectrode materials and their heterostructures would be suitable for photoelectrochemical water splitting.

Introduction

In recent years $BiVO_4$ has been declared as one of the most promising compounds for photo(electro)chemical water oxidation[1], due to its preferential 2.4 eV band gap which allows the absorption of visible light, its suitable valence band position with respect to the O_2/H_2O redox potential, and because it is an inexpensive and non toxic compound made from earth abundant elements. High photocurrents have been demonstrated with $BiVO_4$-based photoanodes under external biases or through coupling to a photovoltaic system. Pihosh et al. demonstrated a water splitting photocurrent of 6.72 mA cm^{-2} under 1 sun illumination at 1.23 V_{RHE} for a $WO_3/BiVO_4$ core-shell nanostructured photoanode with cobalt phosphate (CoPi) as a cocatalyst.[2] When this nanostructured photoanode was coupled to a GaAs/InGaAsP solar cell a solar to hydrogen (STH) generation efficiency of 8.1% was obtained. Qiu et al. found that a nanocone Mo:$BiVO_4$/Fe(Ni)OOH photoanode exhibited a photocurrent density of 5.82 ± 0.36 mA cm^{-2} under 1 sun illumination at 1.23 V_{RHE}.[3] Abdi et al. reported that a 10-step gradient-doped CoPi catalysed W:$BiVO_4$ photoanode could generate an AM 1.5G photocurrent of ~3.6 mA cm^{-2} at 1.23 V vs RHE.[4] When this gradient doped $BiVO_4$ photoanode was combined with a double-junction amorphous silicon solar cell an STH efficiency of 4.9% was obtained. Kim et al. showed that also a stand-alone $BiVO_4$ photoanode could be efficient by obtaining an applied bias photon-to-current efficiency of 1.75% at 0.6 V versus RHE for $BiVO_4$/FeOOH/NiOOH.[5] These reports all indicate that to achieve high water photo-oxidation efficiencies, modifications to bare $BiVO_4$ are required. Hereby, doping with a hexavalent ion like Mo^{6+} or W^{6+} helps to increase the majority charge carrier concentration, nanostructuring helps to reduce the diffusion length and heterostructuring may improve surface passivation, charge carrier separation and water oxidation kinetics.

Heterostructures find their origin in the observation that a singular compound in most cases do not allow for flawless photo(electro)chemical water splitting because that compound is lacking one or more required material properties, that is the ability to absorb a significant fraction of sunlight, to separate charge carriers efficiently and to catalyse the water oxidation and/or reduction reaction with a high reaction rate.[6,7] Practically, photoabsorbers have to be combined with compounds with good electrocatalytic activities.[8] Noble metal

[a] Surface Science Division, Department of Materials Science, Technical University Darmstadt, D-64287 Darmstadt, Germany, E-mail: jaegermann@surface.tu-darmstadt.de; Phone number: +4961511620770
[b] University of Bordeaux, Institut des Sciences Moléculaires, UMR 5255 CNRS, 351 Cours de la Libération, F-33405 Talence Cedex, France
[c] Department of Advanced Materials for Energy, Catalonia Institute for Energy Research (IREC), Jardins de les Dones de Negre, 1, 08930 Sant Adrià de Besòs, Catalonia, Spain
[d] Institute for Solar Fuels, Helmholtz-Zentrum Berlin für Materialien und Energie GmbH, Hahn-Meitner-Platz 1, Berlin 14109, Germany

Electronic Supplementary Information (ESI) available: Bi4$f_{7/2}$ and V2$p_{3/2}$ core level shifts versus thickness, thickness calculation details and contact layer deposition parameters. See DOI: 10.1039/x0xx00000x

based compounds yield good activities for electrocatalytic water oxidation in acidic and basic media, whereas transition metal based compounds generally only exhibit good electrocatalytic water oxidation activities in basic media.[9,10] For $BiVO_4$, mostly cobalt and nickel containing compounds have been found to enhance the water oxidation efficiency, while not many studies can be found that state the same for heterostructures of $BiVO_4$ with noble metal compounds.[2,3,5,11–15]

To this day, the exact benefits of cobalt and nickel containing compounds are still a subject of debate. Some authors claim that cobalt and nickel based compounds enhance the water oxidation catalytic properties of $BiVO_4$.[11,14,16,17] Wang et al. found that the photocurrent density of $BiVO_4$ photoelectrodes could be enhanced by about 4.0 to 4.3 times through coating with, respectively, CoO_x or CoPi.[11] According to the authors, the enhancement was due to a lowering of the activation energy of charge transfer, which they rationalized by the previous finding that cobalt based compounds reduce the overpotential to 0.41 V.[18] The lowering of the overpotential could have a mechanistic background since Co_3O_4 was identified as the electrocatalyst with the lowest theoretical overpotential for the oxygen evolution reaction, based on the optimal binding strength of oxygen to the Co_3O_4 surface, a crucial parameter in the oxygen evolution mechanism.[19] Additionally, cobalt seems to alter its oxidation state during the water oxidation reaction, so that it follows an alternate reaction pathway, which could lead to a lower activation barrier.[20–22] There is, however, no definitive proof that the activation energy is lower, because the exact transition state complexes for this alternate pathway are unknown. Nickel compounds also tend to change the nickel oxidation state during the water oxidation process.[23,24]

Besides insufficient oxidation kinetics, another phenomenon which is said to hamper the performance of metal oxide photoanodes is the presence of electronic surface states.[25,26] Trześniewski et al. suggested the presence of electronic surface states on the $BiVO_4$ surface since they found that the equilibrium potential of untreated $BiVO_4$ lay 0.4 V above the water oxidation potential.[27] Since similar dark equilibrium potentials have been found for TiO_2 and α-Fe_2O_3,[26] a Fermi level pinning mechanism intrinsic to metal oxides immersed in H_2O can be assumed. Passivation of the apparent surface states was presumed to take place when photoanodes were coated with transition metal compounds and/or titania.[28–32] Du et al. observed a reduction of the photocurrent onset potential of hematite when coated with $NiFeO_x$, which they believed originated from surface passivation, because an equilibrium potential was found which was much closer to the water oxidation potential.[29] Zachäus et al. found through a series of intensity modulated photocurrent spectroscopy (IMPS) measurements, which can distinguish between surface recombination and charge carrier injection into the electrolyte, that the low photocurrents of bare $BiVO_4$ photoanodes were due to charge carrier surface recombination at the $BiVO_4$/electrolyte interface, but that the photocurrent could be boosted through the deposition of a very thin ± 1 nm CoPi layer, because CoPi seemed to effectively passivate the $BiVO_4$ surface recombination centers.[33]

Additionally, it must be observed that heterostructures between $BiVO_4$ and other materials with different work functions influence the space charge region in $BiVO_4$, which may alter the bulk charge carrier separation efficiency. For instance, Chang et al. found that the bulk charge transport was improved from 56% for bare $BiVO_4$ to 77% for $BiVO_4$/Co_3O_4.[16] In addition, Barroso et al demonstrated through a series of transient absorption spectroscopy measurements that in the absence of an applied bias electron-hole recombination in hematite photoanodes could be retarded by three orders of magnitude after a thin CoO_x layer was deposited, which the authors attributed to improved charge carrier separation through the formation of a Schottky-type heterojunction.[34]

As outlined above, the exact benefits of heterostructured $BiVO_4$ are not yet completely understood. Indirect techniques, such as IMPS, surface photovoltage spectroscopy (SPS) and transient techniques, have helped to elucidate the effects of a heterostructure, however these techniques were not able to give direct information on the electronic interface band structure and how that affects the contact properties in the photoanode.

In this work alternate thin film sputtering and photoelectron spectroscopy in ultrahigh vacuum (UHV) were used to study heterostructure formation in a direct fashion, allowing interfacial band alignment and the interpretation of charge carrier separation. As such, the junction of $BiVO_4$/NiO, $BiVO_4$/CoO_x and $BiVO_4$/ITO solid/solid interfaces were studied. The exact effect on the $BiVO_4$ electronic and chemical surface structure after interface formation was deduced. Additionally, due to the strongly different work functions of NiO and CoO_x on the one hand and ITO on the other, the extent of Fermi level tuning, change of Fermi level with respect to the band edges, could be investigated by bringing $BiVO_4$ into contact with those materials. As such, bulk Fermi level pinning phenomena could be studied.

Experimental section

Synthesis of $BiVO_4$ thin films

The $BiVO_4$ thin films were prepared through pulsed laser deposition (PLD) according to a previously published procedure.[35] In short, a fluorine-doped tin oxide (FTO) glass (Sigma-Aldrich, TEC 7 Ω/square) substrate was first cleaned with a mixture of acetone/isopropanol/water (1:1:1 %vol) through 10 min of sonication. After drying under a N_2 stream, the substrate was entered into the PLD vacuum chamber and heated to 300 °C under an O_2 pressure of 200 mTorr. The $BiVO_4$ layer was then deposited through ablation of a home-made $BiVO_4$ target with laser pulses at a repetition frequency of 10 Hz, with a total energy set at 150 mJ and an energy fluency of 0.5 J/cm^2. The target-to-substrate distance was set to 90 mm. Approximately 150 nm thick $BiVO_4$ thin films were deposited by selecting the right number of laser pulses. Then, the $BiVO_4$ thin films were post annealed at 500 °C for 3 h in air. The PLD equipment used in this work was a PLD 5000

equipment (PVD Products) with a 240 nm excimer KrF (λ = 248 nm) laser.

Interface formation and analysis

Surface analysis and interface experiments were performed at the Darmstadt Integrated System for Materials research (DAISY-MAT).[36,37] This setup is a combination of several thin film deposition chambers, including atomic layer deposition (ALD), chemical vapour deposition (CVD) and sputtering, and a Physical Electronics PHI 5700 multi-technique surface analysis system to perform Ultraviolet (UPS) and X-ray (XPS) photoelectron spectroscopy. Transferring the samples between the different compartments is possible without breaking the ultra high vacuum (UHV) conditions so that contamination in between deposition and analysis is avoided. XPS measurements were performed using monochromatic Al Kα radiation with an energy resolution of approximately 400meV, determined from the Gaussian broadening of the Fermi edge of a sputter cleaned Ag sample. The Fermi edge of the silver sample was also used to calibrate the binding energies of all photoelectron spectra.

To study the band alignment of $BiVO_4$ in contact with a specific compound, interface experiments were performed. First, the $BiVO_4$ thin film substrates were cleaned with acetone in an ultrasonic bath for 15 minutes, then rinsed with ethanol and water, and subsequently dried using compressed air. Then, the $BiVO_4$ thin film substrates were fixed to a stainless-steel sample holder and entered through a load lock into DAISY-MAT. Remaining organic compounds were removed from the substrate surface with an oxygen plasma treatment of 15 minutes. Then, the interface experiments were performed, whereby the target compound was stepwise sputtered onto the $BiVO_4$ substrate. After each deposition step, core level binding energies of $BiVO_4$ and the sputtered compound were measured via XPS. Additionally, ultraviolet photoelectron (UP) spectra were recorded of the $BiVO_4$ substrate and a thick film of the contact material to determine the secondary electron cut-offs (SECs), which were used to obtain the work functions (WFs) of both materials, according to the formula: WF = hυ – SEC (with hυ equal to 21.2 eV (He I excitation)).[38] The deposition parameters of the investigated contact materials, NiO, CoO_x and Sn-doped In_2O_3 (ITO), can be found in Table S1 and the estimated thickness evolution of the overlayers can be found in Figure S1. NiO and CoO_x were reactively sputtered from a metallic Ni target and a metallic Co target, respectively. ITO was sputtered from a ceramic ITO target with 10 % Sn. All targets had a diameter of 2 inches.

Results and discussion

The $BiVO_4$ thin films, used in this work as the substrates for the interface experiments, were prepared through PLD according to a previously published procedure, whereby XRD measurements have shown that the resulting $BiVO_4$ films are phase pure monoclinic polycrystalline $BiVO_4$ thin films. [35]

In Figure 1,**Error! Reference source not found.** the X-ray photoelectron (XP) spectra for the $BiVO_4$/NiO, $BiVO_4$/CoO_x and $BiVO_4$/ITO interface experiments are plotted for various deposition times. The most relevant energetic values are summarized in Table 1. One can clearly observe the formation of an interface for the three interface experiments since the Bi4f and V2$p_{3/2}$ core level intensities of the $BiVO_4$ substrate decrease and the core level intensities of the contact layer increase with increasing contact layer deposition time (Figure 1). The XP core level spectra at 0 s belong to the bare $BiVO_4$ thin film substrates that were treated by an oxygen plasma treatment. The oxygen plasma treatment is an effective cleaning treatment for ex situ prepared metal oxide samples which can leave behind O_2^- and O_2^{2-} species, due to the strong oxidative nature of the treatment.[39–41] However, in the O1s line of the $BiVO_4$ samples, there is no indication of such peroxides, since these should give rise to an extra signal at a higher binding energy besides the main O^{2-} signal at a binding energy of 529.8 eV.[40] For the bare $BiVO_4$ substrates used in the $BiVO_4$/NiO and $BiVO_4$/ITO interface experiments, a Bi4$f_{7/2}$ binding energy of 159.0 eV was found, which agrees well with the value of Bi^{3+} in $BiVO_4$, while the V2$p_{3/2}$ binding energy found at 516.7 eV matches with V^{5+} in $BiVO_4$.[42] For the $BiVO_4$/CoO_x interface the Bi4$f_{7/2}$ and V2$p_{3/2}$ binding energies are 0.3 eV lower, at 158.7 eV and 516.4 eV respectively. These slightly lower binding energies are most likely due to a shift of the Fermi level, as the $BiVO_4$ valence band maximum (E_F-E_{VBM}) of this substrate is 0.3 eV lower as well, at 1.5 eV, while the other substrates show a VBM of 1.8 eV. Since oxygen vacancies have been cited as a source of unintentional n-type conductivity in metal oxide semiconductors,[43–45] the oxygen plasma treatment could have reduced the number of oxygen vacancies, which led to the lower valence band maximum (E_F-E_{VBM}). Except for NiO, the valence band maxima were obtained from the corresponding XP valence band spectra and are listed in Table 1.

In the first interface experiment NiO was gradually sputtered on top of $BiVO_4$. After a first deposition step of 5 s, a strong upward energy shift of 0.6 eV and a strong decrease in intensity of the Bi4f and V2$p_{3/2}$ core level emissions were observed. The strong decrease in intensity is likely due to a relatively thick NiO film being deposited in the first deposition step. Indeed, based on the attenuation of the V2$p_{3/2}$ and Bi4f photoelectrons a relatively thick 1.3 nm NiO film is deposited after the first deposition step (Figure S1). After the second deposition step, the Bi4f and V2$p_{3/2}$ core level spectra shift by an additional 0.1 eV. Afterwards, no more shifts are observed for further deposition steps. After a total deposition time of 8 min, a rather thick NiO layer has been deposited, resulting in the absence of signal in the Bi4$f_{7/2}$ and V2$p_{3/2}$ spectra. The Ni2p spectrum measured after the last deposition step shows a main line and satellite structure typical for NiO, so that the nickel based overlayer can be assumed to be NiO.[46] In the O1s spectrum after the last deposition step, a main emission line at 529.5 eV and a less intense signal 531.5 eV can be observed. The main line corresponds to the oxygen species in NiO, while

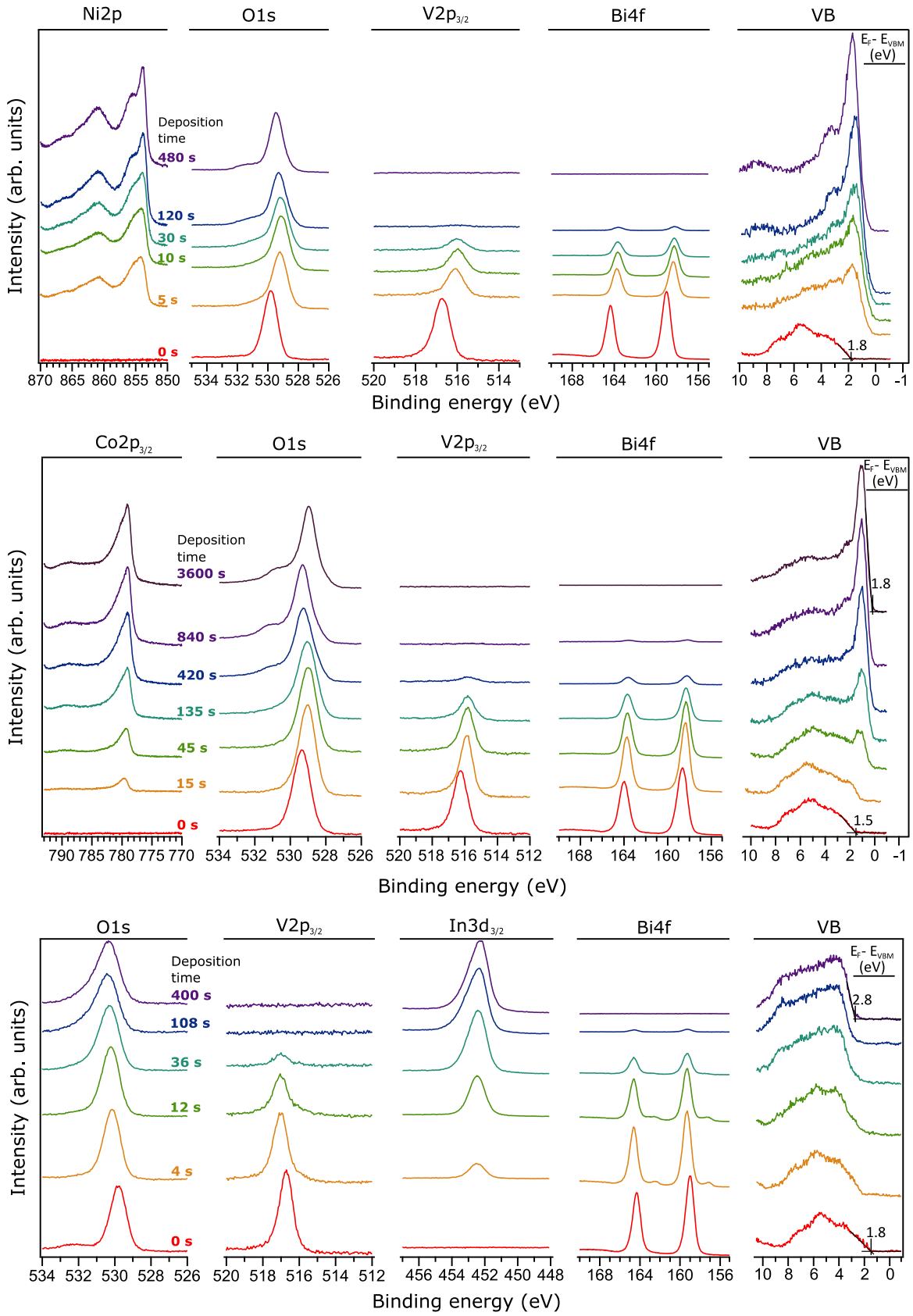

Figure 1: Core level and valence band spectra for the $BiVO_4$/NiO (top), $BiVO_4$/CoO_x (middle) and $BiVO_4$/ITO (bottom) interface experiments. The deposition times for each contact layer are denoted in the core level spectra.

PCCP

ARTICLE

Table 1 Summary of energy values of interface experiments

	$BiVO_4$/NiO	$BiVO_4$/CoO_x	$BiVO_4$/ITO
BE $Bi4f_{7/2}$, 0s (eV)	159.03	158.65	159.00
BE $Bi4f_{7/2}$, final(eV)	158.25	158.22	159.31
BE $V2p_{3/2}$, 0s (eV)	516.71	516.29	516.71
BE $V2p_{3/2}$, final (eV)	515.93	515.82	517.00
Total BE shift (eV)	-0.78	-0.45	0.30
VBM, $BiVO_4$ (eV)	1.8	1.5	1.8
WF, $BiVO_4$ (eV)	5.9	6.6	5.8
VBM, contact layer (eV)	0.4*	0.3	2.8
WF, contact layer (eV)	5.4	5.7	4.5

BE: binding energy; VBM: valence band maximum; WF: work function; 0s: no overlayer deposited yet; final: last spectrum where still enough $Bi4f_{7/2}$ and $V2p_{3/2}$ intensity is to determine the corresponding binding energy; Total shift: mean of total $Bi4f_{7/2}$ and $V2p_{3/2}$ binding energy shift. * Determined from UP spectrum of NiO

the less intense signal at 531.5 eV has been linked to the presence of Ni^{3+}, suggesting a small oxygen overstoichiometry in the NiO film.[47] In the O1s spectrum of other transition metal oxides similar shoulders have been observed, which were ascribed to O^- species and were hypothesized to compensate for defects in transition metal oxide subsurfaces.[48–50]

In the second interface experiment a CoO_x contact layer was stepwise sputtered on top of $BiVO_4$. Similar to the interface with nickel the binding energies in the Bi4f and $V2p_{3/2}$ spectra shift downward with each deposition step. Here, the binding energies shift less drastically due to CoO_x being deposited at a lower rate, which is also noticeable from the $Bi4f_{7/2}$ and $V2p_{3/2}$ line intensities not decreasing strongly after the first deposition step. The $Bi4f_{7/2}$ and $V2p_{3/2}$ binding energies shift by approximately 0.45 eV, seen over all deposition steps. After 1 h of deposition, a sufficiently thick CoO_x layer was obtained, so that the $Bi4f_{7/2}$ and $V2p_{3/2}$ core level could not be detected any more. Co^{2+} and Co^{3+} can be distinguished from each other in the satellite structure of the Co2p spectrum with a Co^{2+} feature being apparent at a binding energy of 786 eV and Co^{3+} at 789 eV.[21,51] Here, both features are clearly visible, which indicates that the deposited cobalt oxide is the mixed oxide CoO_x (with x lying between 1 and 1.5). Similar to the NiO film an extra signal in the O1s core level spectrum can be seen at a binding energy of 531.0 eV for which the same explanation applies as the one stated above.

For the third interface experiment $BiVO_4$ was stepwise covered by an ITO contact layer. Previously, we performed a $BiVO_4$/ITO interface experiment for which we found a downwards band bending of 0.16 eV and a barrier height of 1.96 eV.[52] However, the ITO layer was deposited at room temperature so that the E_F-E_{VBM} was limited to 2.5 eV. Here, $BiVO_4$ was heated to 400 °C before each ITO deposition step, while maintaining a pure argon atmosphere. In this way, the amount of oxygen vacancies in ITO and, thus, the Fermi level position can be increased. Indeed, the E_F-E_{VBM} was now determined to be at 2.8 eV (Figure 1), so that the Fermi level position coincides with the conduction band minimum (CBM), considering an In_2O_3 band gap of 2.8 eV. [53] In contrast to the NiO and CoO_x overlayers, the $Bi4f_{7/2}$ and $V2p_{3/2}$ binding energies shift towards higher values with ITO as a contact layer. There is a shift of 0.30 eV after the first deposition step, after which the Bi4f and $V2p_{3/2}$ binding energies do not shift anymore with further deposition steps. The binding energy at 452.3 eV in the final $In3d_{3/2}$ spectrum is characteristic to ITO.[54]

Additionally, UP spectra were recorded for all $BiVO_4$ thin films and contact materials (Figure 2). The secondary electron cut-offs in the UP spectra were used to determine work functions, which are summarized in Table 1. The work function of the $BiVO_4$ substrates used for the ITO and NiO interfaces can be found at 5.8–5.9 eV, while a 6.6 eV work function was

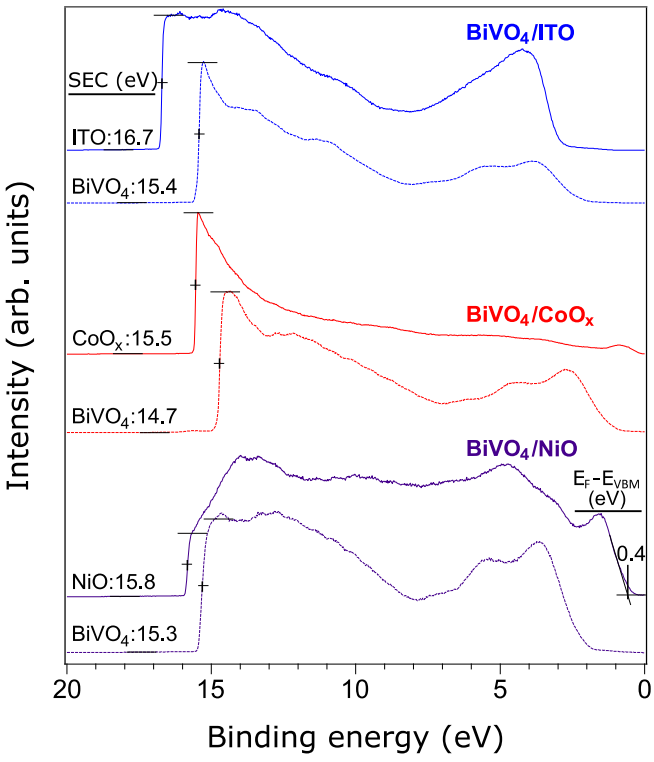

Figure 2: UP spectra (He I excitation) of the $BiVO_4$ substrate and contact layer for the $BiVO_4$/NiO (purple), $BiVO_4$/CoO_x (red) and $BiVO_4$/ITO (blue) interface experiments with the secondary electron cut-offs (SECs) and NiO VBM (E_F-E_{VBM}) depicted in the figure.

found for the substrate used in the $BiVO_4/CoO_x$ interface experiment. Again, this higher work function can be explained by the change of Fermi level position for this substrate, which is also noticeable in the $BiVO_4$ UP spectra. Work functions of 5.4 eV and 5.7 eV were determined for NiO and CoO_x, respectively.

These work functions agree with earlier determined values within our group.[55,56] However, Greiner et al. came up with work functions between 6 eV and 7 eV for NiO and Co_3O_4 after an extensive photoelectron spectroscopic analysis of the first row transition metal oxides.[57] Previously, Greiner et al. found that NiO thin films prepared through in situ oxidation yielded work functions up to 6.7 eV, which, however, dropped below 6.0 eV over time in vacuum, which the authors explained by the adsorption of residual gases in the vacuum.[58] A similar effect could take place on sputtered CoO_x thin films. Additionally, as was explained above, an extra line besides the main O^{2-} line was observed in the O1s spectrum of the CoO_x and NiO thin films, which could be due to O^- species in the subsurface.[48] Reasonably, these species could create a positive dipole at the surface and, thus, be the cause of a lower than expected work function. Since the NiO VBM could not be unambiguously determined from the XP valence band spectrum, the UP spectrum was used instead. A NiO VBM of 0.4 eV was obtained, confirming the p-type character of the NiO film. A 4.5 eV work function was found for ITO, which corresponds to the previously published work functions for ITO.[59,60]

The exact $Bi4f_{7/2}$ and $V2p_{3/2}$ binding energy shifts for all interface experiments are visualized in Figure 3 and the total shifts are listed as well in Table 1. The $Bi4f_{7/2}$ and $V2p_{3/2}$ line maxima for the $BiVO_4$/NiO and $BiVO_4$/ITO interface experiment shift in a similar way, which points to an electronic shift, that is Fermi level position shift, rather than a chemical shift. The shift is less coherent for the $BiVO_4/CoO_x$ interface experiment. First of all, the initial binding energy positions differ from the other

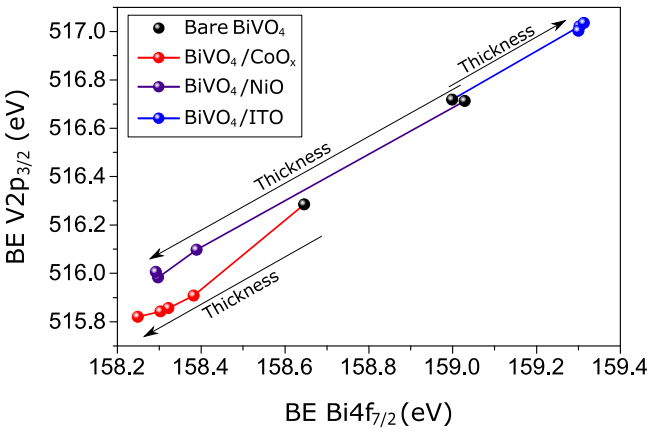

Figure 3: Shift of the $V2p_{3/2}$ and $Bi4f_{7/2}$ binding energies (BE) with respect to the overlayer thickness for the $BiVO_4$/NiO, $BiVO_4/CoO_x$ and $BiVO_4$/ITO interface.

substrates, which, as explained above, is most likely due to a different doping level in that $BiVO_4$ substrate. Additionally, the $Bi4f_{7/2}$ binding energy shift is 40 meV lower than the $V2p_{3/2}$ shift, so that chemical changes during the CoO_x deposition are not unlikely. Since CoO_x was reactively sputtered in an oxygen atmosphere, part of the cobalt ions reaching the $BiVO_4$ could extract oxygen atoms from the surface instead from the sputtering atmosphere. Nevertheless, the 40 meV difference is relatively small compared to the overall 0.45 eV shift, meaning that the observed binding energy shift originates mainly from an electronic shift. Also remarkable is that the binding energy shift for all contact materials is quite abrupt, which indicates that a very thin overlayer (see Figure S1 for thickness estimations) already fixes the electronic properties of the junction.

The electronic shifts can be considered to be the result of band bending at the interface and can be used in combination with the VBMs and WFs listed in Table 1, and the respective band gaps, 2.4 eV for $BiVO_4$,[61] 2.8 eV for ITO,[53] 3.6 eV for NiO[62] and 2.1 eV for CoO_x,[63] to construct interface band diagrams,

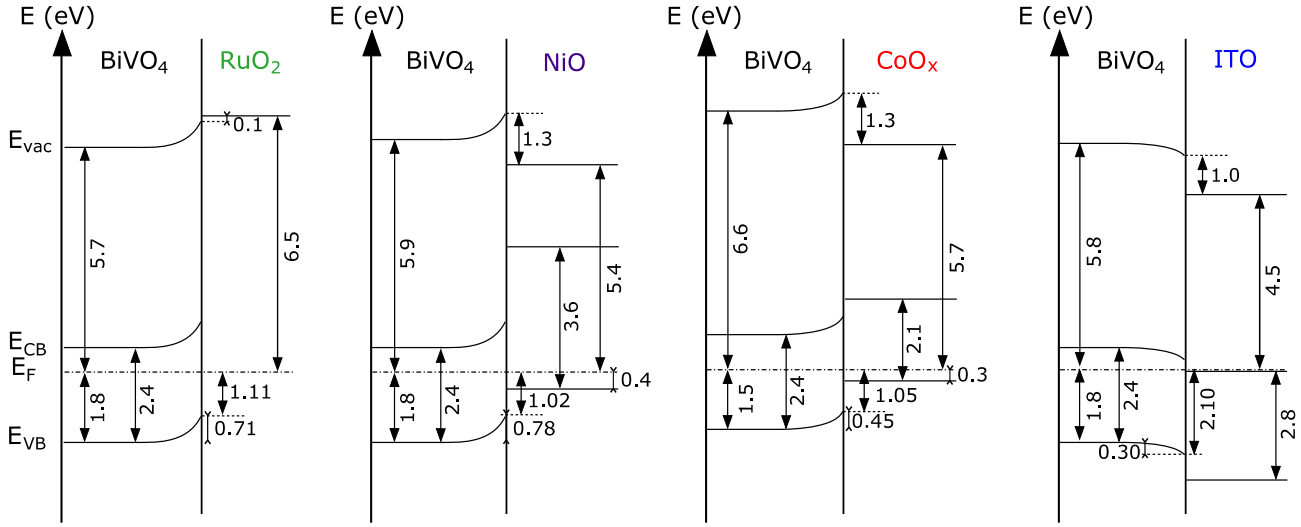

Figure 4: Energy band diagrams of $BiVO_4/RuO_2$, $BiVO_4$/NiO, $BiVO_4/CoO_x$ and $BiVO_4$/ITO interfaces, determined from the combination of X-ray and ultraviolet photoelectron spectroscopy. Band-gap, Fermi level and band edge positions, band bending and barrier heights are shown. All energy values are denoted in eV. The band-gaps of $BiVO_4$, NiO, CoO_x and ITO were taken from literature.[53,61–63] The $BiVO_4/RuO_2$ band diagram is adapted with permission from [52], copyright 2018 American Chemical Society. E_{Vac}, E_{CB}, E_F, E_{VB} represent, respectively, the vacuum level, conduction band minimum, Fermi level and valence band maximum.

which are visualized in Figure 4. There is upwards band bending when $BiVO_4$ forms heterojunctions with NiO and CoO_x, which are high work function materials, and downwards band bending when ITO, which is a low work function material, is the contact layer. From the measured work functions, upwards band bending is not expected for the $BiVO_4$/NiO and $BiVO_4$/CoO_x interfaces. However, the measured NiO and CoO_x work functions could be lower than expected, due to the adsorption of residual gases or due to dipole formation, as explained above.[57,58] At the same time the experimentally determined work function of $BiVO_4$ in this work lies between 5.3–5.9 eV, which is higher than the electron affinity of 4.5–4.8 eV commonly published in literature.[5,64,65] The high value of the work function of $BiVO_4$ could be due to the oxygen plasma treatment, which was used to sputter clean the sample and could create a negative dipole[66,67]. These interface experiments, thus, suggest that the band alignment of a junction cannot be reliably predicted solely from the UPS work functions of the separate components that form the junction, because additional effects due to the processing may strongly modify the outer surface dipole of the individual components. The observation of strong upwards band bending for $BiVO_4$/NiO and $BiVO_4$/CoO_x indicates that the high water oxidation efficiencies obtained with heterostructures of $BiVO_4$ with cobalt and nickel compounds are probably strongly affected by improved charge carrier separation.[2,5] Previous studies confirm this finding. Through a similar combination of XPS and thin film sputtering, the junction between ZnO and NiO was investigated, whereby a band bending value of 0.45 eV was concluded based on the difference in $Zn2p_{3/2}$ binding energy before and after the deposition of a 4.5 nm thick layer of NiO on ZnO.[68] Through transient absorption spectroscopy, Barroso et al. observed that CoO_x could retard charge carrier recombination in hematite by three orders of magnitude due to the formation of a Schottky-type barrier that would improve the charge carrier separation.[34] According to Lin et al. Schottky-type barriers also play a role in the water oxidation mechanism of TiO_2/$Ni(OH)_2$ heterostructures.[23] They observed through double working electrode photoelectrochemistry, which involves two working electrodes that can individually sense or control the potential at the absorber and the electrocatalyst, that the interfacial barrier height increases during oxygen evolution, which they related to the complete oxidation of $Ni(OH)_2$ to NiOOH. Contrarily, Zachäus et al. found through open circuit potential measurements that the band bending in $BiVO_4$ due to CoPi was limited to 0.024 eV.[33] This is in contrast to the 0.45 eV band bending with CoO_x found in this work. The lower band bending could be related to the very thin ± 1 nm CoPi layers that the authors studied, whereby such thin layers could be incomplete and give rise to island formation so that the potential drop could still occur over the $BiVO_4$/electrolyte interface.[22] Differences in open circuit potential can only give an overall estimate of band bending, but not the actual band bending at the local solid state contact between two semiconductors. The important value for the actual charge carrier separation at this contact will depend on the space charge height as well as on the effective recombination rates, whereby both depend on the details of the interface formation. Another thing to note is that the band bending depends on the $BiVO_4$ bulk Fermi level position so that for higher Fermi level positions a stronger band bending and more efficient charge carrier separation is expected for the same heterostructure interface.

The band diagrams in Figure 4 also show how strongly the Fermi level can shift within the band edges, due to the difference in work functions of the contact materials. The $BiVO_4$/ITO interface yields a barrier height of 2.10 eV due to the low work function of ITO, whereas the barrier height for the $BiVO_4$/NiO, $BiVO_4$/CoO_x and $BiVO_4$/RuO_2 amounts to 1.02–1.11 eV, caused by the high work function of these contact materials. In total, the barrier height difference amounts to 1.08 eV. The 1.08 eV barrier height difference

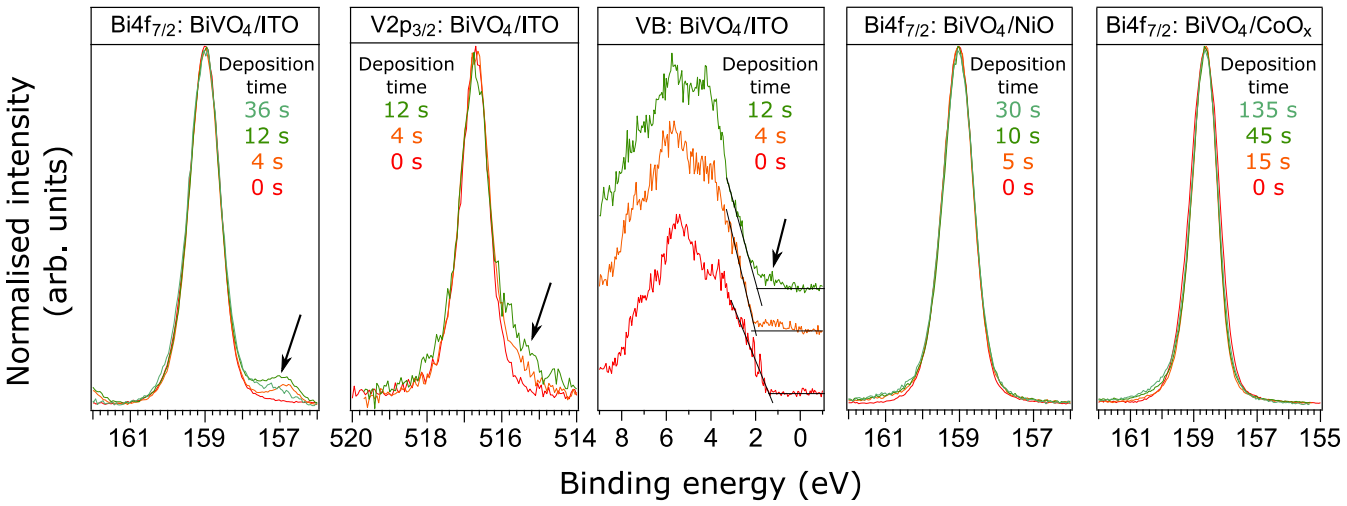

Figure 5: $Bi4f_{7/2}$ spectra for the $BiVO_4$/NiO, $BiVO_4$/CoO_x and $BiVO_4$/ITO interfaces and $V2p_{3/2}$, valence band (VB) spectrum for the $BiVO_4$/ITO interface. For the core level spectra the background was subtracted using a Tougaard function for the Bi4f spectra and a Shirley function for the $V2p_{3/2}$ spectra. Then, the core level spectra were normalized and shifted along the x-axis to align the line maxima. The contact layer deposition times are denoted in the spectra.

indicates that the Fermi level position in $BiVO_4$ can be changed over a wide range without causing any changes in the electronic structure of $BiVO_4$. Fermi level pinning is, thus, unlikely within this 1.08 eV range. To verify that there is no change in the electronic structure in $BiVO_4$, one can take a closer look to the evolution of the $Bi4f_{7/2}$ and $V2p_{3/2}$ core level and valence band XP spectra with respect to the contact layer deposition time, as presented in Figure 5. For the $BiVO_4$/ITO interface a second signal appears at a lower binding energy in both the $V2p_{3/2}$ and $Bi4f_{7/2}$ core level spectra, which is most likely due to partial reduction of the $BiVO_4$ surface. The second signal in the $Bi4f_{7/2}$ spectrum has a binding energy of about 157.0 eV, which corresponds to the binding energy of metallic bismuth.[69] The exact binding energy of the second signal in $V2p_{3/2}$ is more difficult to obtain since V^{5+} can be reduced to V^{4+} or V^{3+} which have similar binding energies. The reduction of V^{5+} and Bi^{3+} could be due to bulk Fermi level pinning, whereby electrons are not placed in the conduction band states, but instead form small polaron states with bismuth and vanadium atoms as the centres of these polaron states. The creation of a small polaron state on a vanadium lattice site after the injection of an electron into the $BiVO_4$ lattice, has been theoretically predicted through DFT calculations with the polaron state having V $3d_{z^2}$ character and was found to be shifted from the conduction band edge into the band gap.[70,71] Furthermore, the localized polaron state has been experimentally verified for molybdenum and tungsten doped $BiVO_4$ single crystals through resonant XPS.[72] Indeed, upon closer inspection of the valence band spectrum after 4 s of ITO deposition (Figure 5) an additional signal appears in the band gap about 0.9 eV from the CBM, the position where the localized polaron state due to V^{4+} would be expected.[70–72] With further ITO deposition the mixing of the ITO and $BiVO_4$ valence band states does not allow further observation of the supposed polaron state.

During the deposition of NiO and CoO_x no significant change in the $Bi4f_{7/2}$ core level spectrum can be observed (Figure 5). There is a small bump appearing at a higher binding energy around 160.5–161.0 eV. This could be due to the oxidation of Bi^{3+} to Bi^{5+}; however since this signal only shows up in a low intensity we could not reliably deduce its existence. In addition, the distinction between Bi^{3+} and Bi^{5+} in Bi4f photoelectron spectra can be vague, as was observed for compounds with mixed bismuth valence states such as $BaBiO_3$.[73–75] For both NiO and CoO_x a similar Schottky-type barrier height between 1.0–1.1 eV is obtained. Similarly, in our previous work we obtained a Schottky-type barrier height of 1.1 eV for the $BiVO_4/RuO_2$ interface.[52] The similarity of these Schottky-type barrier heights strongly indicate that a maximum shift is reached. The reason for this could be Fermi level pinning. Another possibility is that the work function of CoO_x, NiO and RuO_2 is not high enough to obtain further band bending.

Figure 6 summarizes the interface experiments by showing the range over which the $BiVO_4$ Fermi level position can be changed relative to the band positions. Based on the interface experiments, the range over which the Fermi level position can

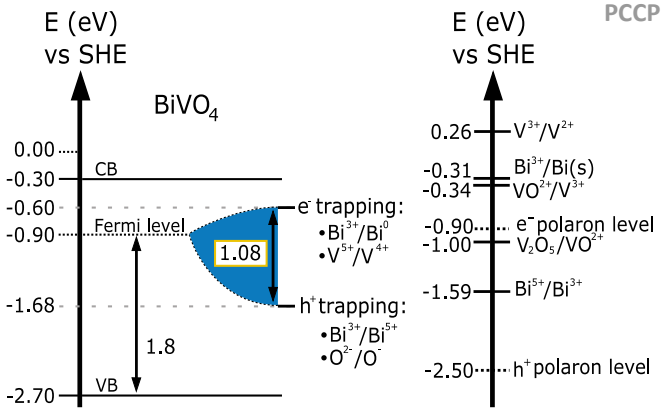

Figure 6: Diagram (left) showing the Fermi level tunability in $BiVO_4$ and the limits based on the obtained information from the interface experiments. The $BiVO_4$ band positions are here taken at the point of zero charge. [82,83] A series of standard redox potentials related to bismuth and vanadium species[80,81] and theoretically determined $BiVO_4$ polaron levels[71] (right) are listed relative to the standard hydrogen electrode potential.

be shifted seems to be limited to 1.08 eV with the lower limit at -1.7 eV vs RHE and the upper limit at -0.6 eV vs RHE. Thus, defects intrinsic to $BiVO_4$ do not prevent water oxidation since the H_2O/O_2 redox potential lie well within the range over which the Fermi level can be changed. Nevertheless, in many occasions Fermi level pinning has been identified as a main reason for poor $BiVO_4$ photoanode efficiency.[33,76–78] However, as has been recently pointed out, various synthesis methods could introduce different native defects, whereby $BiVO_4$ has been mostly synthesized by wet chemical synthesis methods, thus in the presence of water and carbonaceous species.[13,14,78,79] Hence, removing the native carbon and hydroxide layer, as was done in this work through an oxygen plasma treatment, may remove the $BiVO_4$ surface states, which previously have been identified as recombination centres and the cause of Fermi level pinning.

Nevertheless, because of the differing work functions of CoO_x, NiO and RuO_2 the $BiVO_4$ Fermi level limit at -1.7 eV vs SHE may indicate intrinsic defect compensation, involving gap state (polaron) formation, whereby such states could still act as charge carrier recombination centres. The observed lower Fermi level limit at -1.7 eV vs SHE differs, however, strongly from the recently theoretically calculated $BiVO_4$ hole polaron level, lying at -2.5 eV vs SHE.[71] Alternatively, the hole defect compensation level can be estimated from the standard reduction potentials involving bismuth and vanadium. As presented in Figure 6 the Bi^{5+}/Bi^{3+} standard redox potential, which lies at -1.59 eV vs SHE,[80,81] is close to the observed lower Fermi level limit. Similarly, the lower limit at -0.6 eV vs SHE can be due to the intrinsic defect compensation involving reduction of Bi^{3+} and/or V^{5+}. Indeed, indications of Bi^{3+} and V^{5+} reduction could be observed in the XP core level spectra of the $BiVO_4$/ITO interface experiment (Figure 5). The reduction of Bi^{3+} could be linked to the standard redox potential of $Bi^{3+}/Bi(s)$, lying at -0.31 eV vs SHE. Pinpointing the standard redox levels involving V^{5+} is more complicated since the V^{5+}/V^{4+} and V^{4+}/V^{3+} standard redox potentials do not formally exist, possibly due to V^{5+} and V^{4+} being unstable in aqueous electrolytes, wherein these ions form (hydr)oxide based

compounds. Nevertheless, the V^{5+}/V^{4+} and V^{4+}/V^{3+} reduction can be represented by the V_2O_5/VO^{2+} and VO^{2+}/V^{3+} standard redox potential at -1.0 eV vs SHE and -0.34 eV vs SHE.[80,81] The $Bi^{3+}/Bi(s)$, V_2O_5/VO^{2+} and VO^{2+}/V^{3+} standard redox potentials differ, however, from the Fermi level limit at -0.6 eV vs SHE, which may due to the solid state reduction potentials being different from the standard reduction potentials measured in an electrolyte, because of the different coordination of metal ions in an electrolyte compared to a crystal lattice. Additionally, the calculated V^{5+}/V^{4+} polaron level[70,71] lies about 0.3 eV lower than the observed upper Fermi level limit. Further reduction of V^{4+} to V^{3+} may be possible, but the reduction of V^{3+} to V^{2+} is unlikely due to its relatively high standard reduction potential at 0.26 eV vs SHE.

Conclusion

In conclusion, we have demonstrated that the Fermi level position within $BiVO_4$ can be effectively tuned over a range of 1.1 eV through the formation of junctions with high and low work function materials. High upwards band bending, 0.45 eV and 0.78 eV for $BiVO_4/CoO_x$ and $BiVO_4$/NiO, respectively, indicate that high work function transition metal oxides may play important role in the separation of charge carriers upon light absorption. Additionally, Fermi level pinning seems to be limited for decreasing E_F-E_{VBM}, which would explain the intrinsic electronic stability of $BiVO_4$ at anodic potentials. For increasing E_F-E_{VBM}, as probed by contacting BiVO4 at elevated temperature with a low work function material, ITO, Fermi level pinning seems to take place at E_F-E_{VBM} > 2.0–2.1 eV since a reduction of bismuth and vanadium was observed when the $BiVO_4$/ITO contact was established. This Fermi level pinning state has most probably no severe implications for reduction reactions in photoelectrochemical cells since $BiVO_4$ is usually not subjected to cathodic potentials. However, it may limit the effective n-type doping concentration which can be attained by adding electron donating elements. Future interface experiments could focus on the band alignment of contact materials with specific crystalline facets of $BiVO_4$ to elucidate whether surface structure has a strong influence on the contact properties. Furthermore, promising photoelectrode candidates could be studied in a similar way to identify whether they will be able to achieve high efficiencies for photoelectrochemical water splitting and if certain contact materials could improve the contact properties.

Conflicts of interest

There are no conflicts to declare.

Acknowledgements

This work was carried out in the framework of EJD-FunMat (European Joint Doctorate for Multifunctional Materials) and has received funding from the European Union's Horizon 2020 research and innovation programme under the Marie Sklodowska-Curie grant agreement No 641640. In addition, the authors from IREC thank Generalitat de Catalunya for financial support through the CERCA Program and M2E (2017SGR1246), and support by the European Regional Development Funds (ERDF, FEDER) and MINECO project ENE2017-85087-C3-2-R. S.M.-L. thanks European Union's Horizon 2020 and the Agency for Business Competitiveness of the Government of Catalonia for funding under the Marie Sklodowska-Curie grant agreement No. 712939 (TECNIOspring PLUS).

Notes and references

1 K. Sivula and R. Van De Krol, *Nat. Rev. Mater.*, 2016, **1**, 15010.

2 Y. Pihosh, I. Turkevych, K. Mawatari, J. Uemura, Y. Kazoe, S. Kosar, K. Makita, T. Sugaya, T. Matsui, D. Fujita, M. Tosa, M. Kondo and T. Kitamori, *Sci. Rep.*, 2015, **5**, 11141.

3 Y. Qiu, W. Liu, W. Chen, G. Zhou, P. C. Hsu, R. Zhang, Z. Liang, S. Fan, Y. Zhang and Y. Cui, *Sci. Adv.*, 2016, **2**, e1501764.

4 F. F. Abdi, L. Han, A. H. M. Smets, M. Zeman, B. Dam and R. Van De Krol, *Nat. Commun.*, 2013, **4**, 17594–17598.

5 T. W. Kim and K.-S. Choi, *Science (80-.).*, 2014, **343**, 990–994.

6 S. Giménez and J. Bisquert, *Photoelectrochemical Solar Fuel Production*, Springer International Publishing, Cham, 2016.

7 W. Jaegermann, B. Kaiser, J. Ziegler and J. Klett, in *Photoelectrochemical Solar Fuel Production*, Springer International Publishing, Cham, 2016, pp. 199–280.

8 A. Kudo and Y. Miseki, *Chem. Soc. Rev.*, 2009, **38**, 253–278.

9 C. C. L. McCrory, S. Jung, J. C. Peters and T. F. Jaramillo, *J. Am. Chem. Soc.*, 2013, **135**, 16977–16987.

10 C. C. L. McCrory, S. Jung, I. M. Ferrer, S. M. Chatman, J. C. Peters and T. F. Jaramillo, *J. Am. Chem. Soc.*, 2015, **137**, 4347–4357.

11 D. Wang, R. Li, J. Zhu, J. Shi, J. Han, X. Zong and C. Li, *J. Phys. Chem. C*, 2012, **116**, 5082–5089.

12 R. Li, H. Han, F. Zhang, D. Wang and C. Li, *Energy Environ. Sci.*, 2014, **7**, 1369–1376.

13 F. F. Abdi, N. Firet and R. vandeKrol, *ChemCatChem*, 2013, **5**, 490–496.

14 M. Zhong, T. Hisatomi, Y. Kuang, J. Zhao, M. Liu, A. Iwase, Q. Jia, H. Nishiyama, T. Minegishi, M. Nakabayashi, N. Shibata, R. Niishiro, C. Katayama, H. Shibano, M. Katayama, A. Kudo, T. Yamada and K. Domen, *J. Am. Chem. Soc.*, 2015, **137**, 5053–5060.

15 Q. Wang, T. Hisatomi, Q. Jia, H. Tokudome, M. Zhong, C. Wang, Z. Pan, T. Takata, M. Nakabayashi, N. Shibata, Y. Li, I. D. Sharp, A. Kudo, T. Yamada and K. Domen, *Nat. Mater.*, 2016, **15**, 611–615.

16 X. Chang, T. Wang, P. Zhang, J. Zhang, A. Li and J. Gong, *J. Am. Chem. Soc.*, 2015, **137**, 8356–8359.

17 S. K. Choi, W. Choi and H. Park, *Phys. Chem. Chem. Phys.*, 2013, **15**, 6499.

18 M. W. Kanan and D. G. Nocera, *Science (80-.).*, 2008, **321**, 1072–1075.

19 I. C. Man, H. Y. Su, F. Calle-Vallejo, H. A. Hansen, J. I.

Martínez, N. G. Inoglu, J. Kitchin, T. F. Jaramillo, J. K. Nørskov and J. Rossmeisl, *ChemCatChem*, 2011, **3**, 1159–1165.

20 D. K. Zhong, S. Choi and D. R. Gamelin, *J. Am. Chem. Soc.*, 2011, **133**, 18370–18377.

21 N. Weidler, S. Paulus, J. Schuch, J. Klett, S. Hoch, P. Stenner, A. Maljusch, J. Brötz, C. Wittich, B. Kaiser and W. Jaegermann, *Phys. Chem. Chem. Phys.*, 2016, **18**, 10708–10718.

22 T. H. Jeon, W. Choi and H. Park, *Phys. Chem. Chem. Phys.*, 2011, **13**, 21392–21401.

23 F. Lin and S. W. Boettcher, *Nat. Mater.*, 2014, **13**, 81–86.

24 N. Weidler, J. Schuch, F. Knaus, P. Stenner, S. Hoch, A. Maljusch, R. Schäfer, B. Kaiser and W. Jaegermann, *J. Phys. Chem. C*, 2017, **121**, 6455–6463.

25 B. Klahr and T. Hamann, *J. Phys. Chem. C*, 2014, **118**, 10393–10399.

26 C. Du, M. Zhang, J.-W. Jang, Y. Liu, G.-Y. Liu and D. Wang, *J. Phys. Chem. C*, 2014, **118**, 17054–17059.

27 B. J. Trześniewski and W. A. Smith, *J. Mater. Chem. A*, 2016, **4**, 2919–2926.

28 O. Zandi and T. W. Hamann, *J. Phys. Chem. Lett.*, 2014, **5**, 1522–1526.

29 C. Du, X. Yang, M. T. Mayer, H. Hoyt, J. Xie, G. McMahon, G. Bischoping and D. Wang, *Angew. Chemie Int. Ed.*, 2013, **52**, 12692–12695.

30 M. T. McDowell, M. F. Lichterman, J. M. Spurgeon, S. Hu, I. D. Sharp, B. S. Brunschwig and N. S. Lewis, *J. Phys. Chem. C*, 2014, **118**, 19618–19624.

31 X. Yang, R. Liu, C. Du, P. Dai, Z. Zheng and D. Wang, *ACS Appl. Mater. Interfaces*, 2014, **6**, 12005–12011.

32 Y. Liang and J. Messinger, *Phys. Chem. Chem. Phys.*, 2014, **16**, 12014.

33 C. Zachäus, F. F. Abdi, L. M. Peter and R. Van De Krol, *Chem. Sci.*, 2017, **8**, 3712–3719.

34 M. Barroso, A. J. Cowan, S. R. Pendlebury, M. Grätzel, D. R. Klug and J. R. Durrant, *J. Am. Chem. Soc.*, 2011, **133**, 14868–14871.

35 S. Murcia-López, C. Fàbrega, D. Monllor-Satoca, M. D. Hernández-Alonso, G. Penelas-Pérez, A. Morata, J. R. Morante and T. Andreu, *ACS Appl. Mater. Interfaces*, 2016, **8**, 4076–4085.

36 A. Klein, *J. Am. Ceram. Soc.*, 2013, **96**, 331–345.

37 A. Klein, *J. Am. Ceram. Soc.*, 2016, **99**, 369–387.

38 M. Cardona and L. Ley, *Photoemission in Solids I : General Principles*, Springer Berlin Heidelberg, 1978.

39 H. Y. Yu, X. D. Feng, D. Grozea, Z. H. Lu, R. N. S. Sodhi, A.-M. Hor and H. Aziz, *Appl. Phys. Lett.*, 2001, **78**, 2595–2597.

40 X.-Q. Deng, B. Zhu, X.-S. Li, J.-L. Liu, X. Zhu and A.-M. Zhu, *Appl. Catal. B Environ.*, 2016, **188**, 48–55.

41 W. Hu, M. Matsumura, K. Furukawa and K. Torimitsu, *J. Phys. Chem. B*, 2004, **108**, 13116–13118.

42 L. Chen, E. Alarcón-Lladó, M. Hettick, I. D. Sharp, Y. Lin, A. Javey and J. W. Ager, *J. Phys. Chem. C*, 2013, **117**, 21635–21642.

43 A. Janotti, J. B. Varley, P. Rinke, N. Umezawa, G. Kresse and C. G. Van de Walle, *Phys. Rev. B*, 2010, **81**, 085212.

44 T. W. Kim, Y. Ping, G. A. Galli and K.-S. Choi, *Nat. Commun.*, 2015, **6**, 8769.

45 H. Tan, Z. Zhao, W. Zhu, E. N. Coker, B. Li, M. Zheng, W. Yu, H. Fan and Z. Sun, *ACS Appl. Mater. Interfaces*, 2014, **6**, 19184–19190.

46 A. P. Grosvenor, M. C. Biesinger, R. S. C. Smart and N. S. McIntyre, *Surf. Sci.*, 2006, **600**, 1771–1779.

47 S. Oswald and W. Brückner, *Surf. Interface Anal.*, 2004, **36**, 17–22.

48 J.-C. Dupin, D. Gonbeau, P. Vinatier and A. Levasseur, *Phys. Chem. Chem. Phys.*, 2000, **2**, 1319–1324.

49 T. J. Chuang, C. R. Brundle and D. W. Rice, *Surf. Sci.*, 1976, **59**, 413–429.

50 V. M. Jiménez, A. Fernández, J. P. Espinós and A. R. González-Elipe, *J. Electron Spectros. Relat. Phenomena*, 1995, **71**, 61–71.

51 M. C. Biesinger, B. P. Payne, A. P. Grosvenor, L. W. M. Lau, A. R. Gerson and R. S. C. Smart, *Appl. Surf. Sci.*, 2011, **257**, 2717–2730.

52 Y. Hermans, A. Klein, K. Ellmer, R. van de Krol, T. Toupance and W. Jaegermann, *J. Phys. Chem. C*, 2018, **122**, 20861–20870.

53 A. Walsh, J. L. F. Da Silva, S. H. Wei, C. Körber, A. Klein, L. F. J. Piper, A. Demasi, K. E. Smith, G. Panaccione, P. Torelli, D. J. Payne, A. Bourlange and R. G. Egdell, *Phys. Rev. Lett.*, 2008, **100**, 167402.

54 A. Kachouane, M. Addou, A. Bougrine, B. El idrissi, R. Messoussi, M. Regragui and J. C. Bérnede, *Mater. Chem. Phys.*, 2001, **70**, 285–289.

55 S. Tengeler, M. Fingerle, W. Calvet, C. Steinert, B. Kaiser, T. Mayer and W. Jaegermann, *J. Electrochem. Soc.*, 2018, **165**, H3122–H3130.

56 C. Lohaus, J. Morasch, J. Brötz, A. Klein and W. Jaegermann, *J. Phys. D. Appl. Phys.*, 2016, **49**, 155306.

57 M. T. Greiner, L. Chai, M. G. Helander, W. M. Tang and Z. H. Lu, *Adv. Funct. Mater.*, 2012, **22**, 4557–4568.

58 M. T. Greiner, M. G. Helander, Z. Bin Wang, W. M. Tang and Z. H. Lu, *J. Phys. Chem. C*, 2010, **114**, 19777–19781.

59 Y. Park, V. Choong, Y. Gao, B. R. Hsieh and C. W. Tang, *Appl. Phys. Lett.*, 1996, **68**, 2699–2701.

60 Y. Gassenbauer and A. Klein, *J. Phys. Chem. B*, 2006, **110**, 4793–4801.

61 S. Tokunaga, H. Kato and A. Kudo, *Chem. Mater.*, 2001, **13**, 4624–4628.

62 M. D. Irwin, D. B. Buchholz, A. W. Hains, R. P. H. Chang and T. J. Marks, *Proc. Natl. Acad. Sci.*, 2008, **105**, 2783–2787.

63 J. M. Xu and J. P. Cheng, *J. Alloys Compd.*, 2016, **686**, 753–768.

64 J. K. Cooper, S. Gul, F. M. Toma, L. Chen, P. A. Glans, J. Guo, J. W. Ager, J. Yano and I. D. Sharp, *Chem. Mater.*, 2014, **26**, 5365–5373.

65 J. Su, X.-X. Zou, G.-D. Li, X. Wei, C. Yan, Y.-N. Wang, J. Zhao, L.-J. Zhou and J.-S. Chen, *J. Phys. Chem. C*, 2011, **115**, 8064–8071.

66 K. S. Kim, K. H. Lee, K. Cho and C. E. Park, *J. Memb. Sci.*, 2002, **199**, 135–145.

67 F.-L. Kuo, Y. Li, M. Solomon, J. Du and N. D. Shepherd, *J.*

Phys. D. Appl. Phys., 2012, **45**, 065301.

68 Z. G. Yang, L. P. Zhu, Y. M. Guo, W. Tian, Z. Z. Ye and B. H. Zhao, *Phys. Lett. Sect. A Gen. At. Solid State Phys.*, 2011, **375**, 1760–1763.

69 J. F. Moulder, W. F. Stickle, P. E. Sobol and K. D. Bomben, *Handbook of X-ray photoelectron spectroscopy: a reference book of standard spectra for identification and interpretation of XPS data*, Physical Electronics, Eden Prairie MN, 1992.

70 K. E. Kweon, G. S. Hwang, J. Kim, S. Kim and S. Kim, *Phys. Chem. Chem. Phys.*, 2015, **17**, 256–260.

71 J. Wiktor, F. Ambrosio and A. Pasquarello, *ACS Energy Lett.*, 2018, **3**, 1693–1697.

72 V. Jovic, J. Laverock, A. J. E. Rettie, J.-S. Zhou, C. B. Mullins, V. R. Singh, B. Lamoureux, D. Wilson, T.-Y. Su, B. Jovic, H. Bluhm, T. Söhnel and K. E. Smith, *J. Mater. Chem. A*, 2015, **3**, 23743–23753.

73 A. Winiarski, G. Wübbeler, C. Scharfschwerdt, E. Clausing and M. Neumann, *Fresenius. J. Anal. Chem.*, 1991, **341**, 296–300.

74 M. Nagoshi, T. Suzuki, Y. Fukuda, K. Ueki, A. Tokiwa, M. Kiruchi, Y. Syono and M. Tachiki, *J. Phys. Condens. Matter*, 1992, **4**, 5769–5781.

75 A. S. Chouhan, E. Athresh, R. Ranjan, S. Raghavan and S. Avasthi, *Mater. Lett.*, 2018, **210**, 218–222.

76 Q. Shi, S. Murcia-López, P. Tang, C. Flox, J. R. Morante, Z. Bian, H. Wang and T. Andreu, *ACS Catal.*, 2018, **8**, 3331–3342.

77 B. Pattengale and J. Huang, *Phys. Chem. Chem. Phys.*, 2017, **19**, 6831–6837.

78 B. Lamm, B. J. Trześniewski, H. Döscher, W. A. Smith and M. Stefik, *ACS Energy Lett.*, 2017, **3**, acsenergylett.7b00834.

79 X. Shi, I. Y. Choi, K. Zhang, J. Kwon, D. Y. Kim, J. K. Lee, S. H. Oh, J. K. Kim and J. H. Park, *Nat. Commun.*, 2014, **5**, 4775.

80 G. Milazzo, S. Caroli, V. K. Sharma and International Union of Pure and Applied Chemistry. Electrochemistry Commission., *Tables of standard electrode potentials*, Wiley, London, 1978.

81 A. J. Bard, R. Parsons, J. Jordan and International Union of Pure and Applied Chemistry., *Standard potentials in aqueous solution*, Dekker, New York, 1985.

82 H. Jiang, M. Nagai and K. Kobayashi, *J. Alloys Compd.*, 2009, **479**, 821–827.

83 H. Li, G. Liu and X. Duan, *Mater. Chem. Phys.*, 2009, **115**, 9–13.